High dielectric 3D scaffold to suppress Li-dendrites and increase the reversibility of anode-less Li-metal anodes

Chao Wang
Delft University of Technology

Ming Liu
Delft University of Technology

Michel Thijs
Delft University of Technology

Frans Ooms
Delft University of Technology

Swapna Ganapathy
Department of Radiation Science and Technology, Delft University of Technology
https://orcid.org/0000-0001-5265-1663

Marnix Wagemaker (✉ m.wagemaker@tudelft.nl)
Department of Radiation Science and Technology, Delft University of Technology
https://orcid.org/0000-0003-3851-1044

High dielectric 3D scaffold to suppress Li-dendrites and increase the reversibility of anode-less Li-metal anodes

Chao Wang[1], Ming Liu[1], Michel Thijs[2], Frans G.B. Ooms[1], Swapna Ganapathy[1] and Marnix Wagemaker[1*]

[1] Section Storage of Electrochemical Energy, Radiation Science and Technology, Faculty of Applied Sciences, Delft University of Technology. E-mail: m.wagemaker@tudelft.nl

[2] Neutron & Positron Methods for Materials, Radiation Science and Technology, Faculty of Applied Sciences, Delft University of Technology.

ABSTRACT

The lithium metal anode is intensively investigated because it considerably increases Li-battery energy density. However, the formation of dendritic/mossy Li-metal microstructures amplifies electrolyte decomposition and Li deactivation. Here we investigate the impact of a high-dielectric porous scaffold, aiming to eliminate the fundamental driver for dendritic/mossy Li-metal growth, the large electrical field gradients at inhomogeneities at the anode surface. In an anode-less (Li-metal free) high-dielectric porous scaffold, this promotes dense plating as observed by operando solid-state NMR. Even in a simple carbonate electrolyte, 1M $LiPF_6$ in EC/DMC, the high-dielectric scaffold improves the plating/stripping efficiency up to 99.82%, extending the cycle life, indicating that electrolyte decomposition is minimized by the induced compact Li-metal plating. The large porosity of the scaffolds, non-optimized and easy to prepare, enables a specific capacity beyond 2000 mA h g^{-1}, presenting a facile approach to promote compact Li-metal plating to improve Li-metal anode efficiency and safety.

The development of high energy density batteries beyond current Li-ion battery technology is necessary to meet the increasing demand for mobile applications such as electric vehicles.[1-5] Lithium metal is considered the ultimate anode material because it possesses the highest theoretical specific capacity, 3860 mA h g^{-1}, approximately ten times that of current graphite-based anodes, and low redox potential that endows it with a high battery output voltage (-3.040 V vs standard hydrogen electrode).[6-10] However, upon repeated battery charging and discharging, the plating and stripping of Li-metal induces irreversible processes that lead to fast capacity decay which drastically limits the Li-metal battery cycle life.[6-10] The formation of high surface area dendritic and mossy Li-metal morphologies, in combination with the vicious reactivity of Li-metal towards common electrolytes, leads to an irreversible loss of active Li towards solid electrolyte interface products as well as the formation of inactive Li-metal. The latter is often referred to as "dead" Li, which has lost contact with the current collector.[11-14] Additionally, dendritic structures may penetrate the separator/electrolyte and reach the cathode, causing an internal short-circuit that may induce rapid spontaneous discharge and consequential safety hazards.[6-10] Loss of active Li is in research cells often masked by the excess of Li-metal present, but in practical cells, the amount of excess Li should be minimized to maximize the energy density.[15] Ultimately, all active Li is stored in the cathode in the discharged state. This so-called "anode-less" or "anode free" design, has the additional advantage of not necessitating Li-metal handling.

Strategies that aim to suppress, prevent and block dendrite formation are intensively investigated,[6-10,16,17] typically guided by our current understanding of dendrite nucleation and growth. The space charge model of Chazalviel predicts that when the Li-ion concentration on the surface of the anode drops to zero, after the

characteristic Sand's time, plating becomes inhomogeneous and self-amplified growth of dendrites is induced.[18] This motivates the use of strategies that enhance ion mobility, increase the transference number and introduce a large anode surface area to promote a homogenous Li-ion flux and to prevent ion depletion at the anode surface.[6-10,16,17] Modelling of the early stages of nucleation and growth under heterogeneous electrodeposition indicates that the anode surface inhomogeneities, particle size and wettability play a critical role in facilitating dendrite formation.[19] This implies that dendrite growth can be steered by controlling these parameters on the anode, as experimentally demonstrated.[20] The comparison with Mg metal, that does not favour dendrite formation, indicates that both the high surface diffusion barriers for Li and the low surface energy density promote dendrite formation. This is because Li-metal diffusion away from the tip where it is initially deposited is hindered and large surface area morphologies are allowed.[21] To regulate these issues, strategies are employed which aim to control the Li-metal-electrolyte interface via the SEI composition.[22] Residual stress within the Li-metal appears to be another driving force for Li-metal growth.[23] This motivates the design of substrates that can release this stress.[10,23] Finally, investigations of how mechanical forces affect dendrite nucleation and growth, have shown that electrolytes with a shear modules, at least 2 times larger than that of Li-metal, can prevent dendrite growth.[24] This has given rise to research where mechanically strong separators, solid electrolytes and protective films are investigated. [6-10,16,17]

3D scaffolds are an interesting approach, as they provide the possibility to control the interface, the local interface environment and to a large extent the charge transport. They can also provide a route to mitigate delamination due to their ability to accommodate large volumetric changes upon Li-metal plating and stripping. In a 3D

scaffold that is electronically conducting, the electric field is roughly uniform and the local current density is reduced, suppressing dendrite growth.[25-30] However, the 3D porous conductive matrix is equipotential, due to which Li-metal can also be deposited on top of the 3D matrix, thus negating its targeted function.[31]

Here we explore an alternative approach through the introduction of a material with a high dielectric constant (which we will refer to as a high dielectric material) as a 3D scaffold. Due to the polarizing power of high dielectric material, an effective immobile surface (space) charge density ρ_{charge} is established, opposing the applied field in the battery (ferroelectric effect), that scales with the dielectric constant ($\nabla \cdot D = \rho_{charge}$ where $D = \varepsilon_0 \varepsilon_r E$, ε_0 and ε_r the vacuum and relative permittivity and E the electrical field). As a consequence, the electrical field lines are drawn towards the high dielectric material (dictated by Gauss Law) which leads to lowering of the divergence of the electrical field in the vicinity of the Li-metal deposition. At the tip of a dendrite near a high dielectric material, this effectively leads to a decrease in the electrical field divergence, and thus to a lower local electrical field gradient. This is shown in **Figure 1**, where the calculated electrical field gradient near a dendrite with, and without high dielectric volumes in the vicinity of a dendrite are compared. This is proposed to lower the driving force for the plating of Li-ions at the tip of an inhomogeneity near to the high dielectric material. Indeed more homogeneous deposits have been recently observed, due to the presence of high dielectric materials.[32] Based on this simple principle, we prepared porous 3D barium titanate (henceforth denoted as BTO) scaffolds which have an ultra-high dielectric constant. The impact of this high dielectric based 3D scaffold is examined by direct comparison with an Al_2O_3 3D scaffold having a low dielectric constant and a comparable 3D scaffold morphology. These Li-metal free scaffolds (anode-less) are cycled versus a Li-metal anode to evaluate the Li-metal

morphology and cycling efficiency. To highlight the impact of this approach, cycling is performed in combination with a conventional electrolyte (1M LiPF$_6$ in 1:1 v/v EC: DMC), presenting the worst-case scenario as this electrolyte is well known for leading to uncontrolled SEI formation. In combination with the high dielectric BTO scaffold, this results in a Coulombic Efficiency (CE) in excess of 99.82% and small overpotentials of 68 mV, reaching 320 cycles in half cells at 2 mA cm^{-2} cycled to 1 mA h cm^{-2}. In addition, when combined with an NMC cathode, the BTO scaffold anode leads to a strongly improved CE and cycle life. Its high porosity, ~60%, leads to a specific capacity of more than 2000 mA h g^{-1}, taking into account the weight of the 3D scaffold. The high relative permittivity is shown to suppress dendrite growth, promote homogeneous plating, thus damping the self-amplifying cycle of SEI formation and dendritic growth. Nevertheless, several challenges remain, one of which is the reactivity of the scaffold. Though very limited, it contributes to the initial capacity loss, and the cycling of these anodeless scaffolds, still appears to terminate via a short circuit. This prompts the investigation of combinatorial approaches, especially utilizing optimized electrolytes and binders to improve performance. The proposes scaffolds are attractive from a practical standpoint, as they are prepared by means of regular electrode casting. Thereby, the proposed strategy presents new insights into the role of the permittivity on Li-metal deposition and a promising approach for the design of (anode-less) scaffolds to achieve efficient Li-metal anodes.

Results and Discussion

Electrical field calculations. To understand the impact of the dielectric constant of a dielectric block on the electrical field gradient at a nearby Li-metal dendrite, the electrical field is simulated in two dimensions. This is performed for both a bare Cu

current collector with a Li-metal dendrite, and a Cu current collector in combination with high dielectric BaTiO$_3$ (BTO) and low dielectric Al$_2$O$_3$ (AO) blocks surrounding the dendrite as shown in **Figure 1**. The relative permittivity's of BTO, AO and the electrolyte are 4000, 8 and 40, respectively.
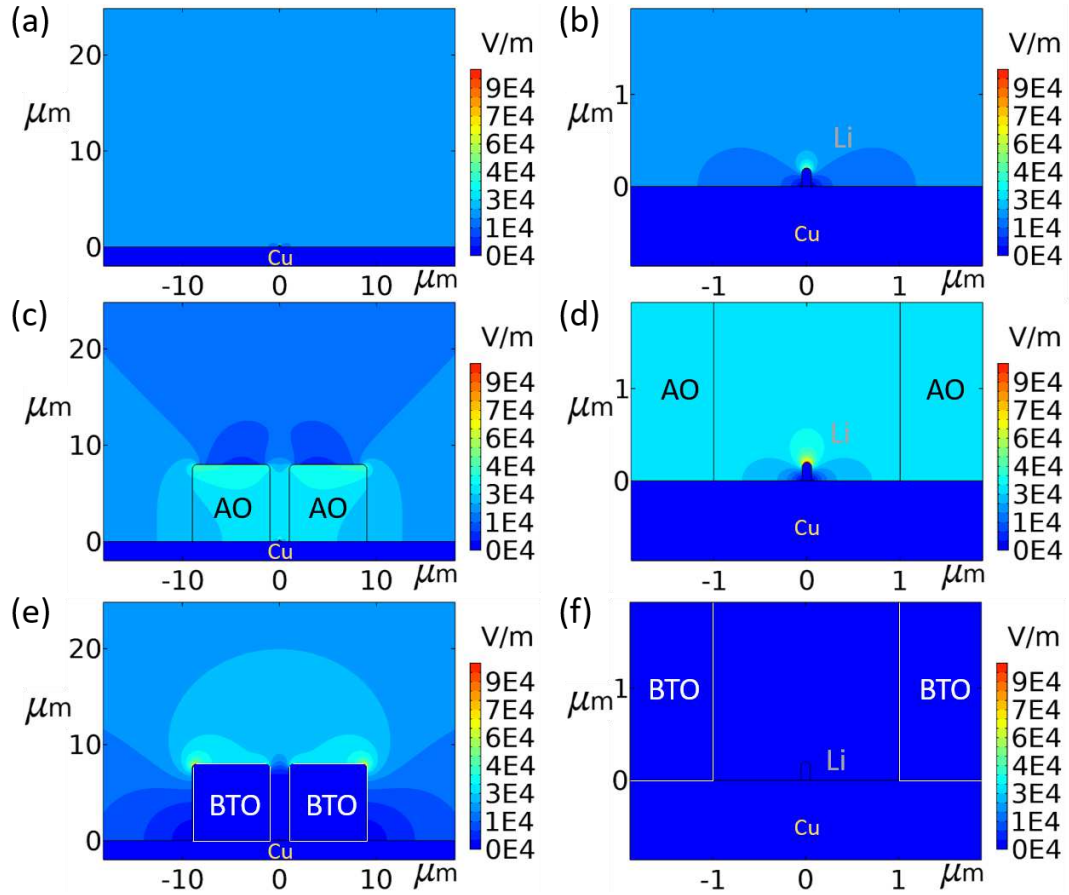

Figure 1 Electrical field simulations around a Li-metal deposit with and without the presence of low and high dielectric blocks. Li-metal deposit (a) on bare Cu planar copper and (b) zoomed-in figure, (c) in combination with low dielectric AO block (d) zoomed-in figure, (e) in combination with high dielectric BTO block (f) zoomed-in figure.

These Cu, BTO/Cu and AO/Cu electrodes are placed against a counter electrode at a distance of 250 μm separated by the electrolyte to approximate the situation in a battery. The BTO and AO blocks are taken as 8 μm x 8 μm with a gap of 2 μm in which a lithium dendrite is placed, represented by a rectangular shape (0.1 μm x 0.2 μm) with a hemispherical tip. In **Figure 1a** and **1b**, the simulated electrical field around a single dendrite in the electrolyte is shown. Near the tip of the Li-metal,

6

the electrical field gradient increases, demonstrating that the electrical field lines are focused to the tip of the electronically conducting Li-metal dendrite. This is driven by the larger surface charge density present at the sharp electronically conducting features. This promotes the preferential deposition of Li-ions from the electrolyte on the tip of the dendrite, representing the fundamental driving force for dendrite formation in a homogeneous medium. As shown in **Figure 1c** and **1d**, blocks of AO (relative permittivity 8, smaller than that of the electrolyte) and in **Figure 1e** and **1f**, blocks of BTO (relative permittivity 4000, much higher than that of the electrolyte) are added on both sides of the Li-dendrite. For AO, the electrical field gradient near the tip of the dendrite increases (**Figure 1d**) when compared to its presence in the electrolyte alone (**Figure 1b**), whereas for BTO, the electrical field gradient at the tip of the dendrite disappears (**Figure 1e**). The low polarizability of the AO "leaves" the electrical field gradient at the Li-metal tip, whereas the high polarizability of the BTO "pulls" the electrical field lines away from the Li-metal tip towards the surface of the BTO itself. This suggests that the presence of high dielectric blocks in the vicinity of a Li-metal growth takes away the driving force for Li deposition at the tip of sharp features, thus taking away the driving force for tip driven dendrite growth. Several geometries were simulated, such as different block distances, different dendrite lengths to name a few, provided in the Supplementary Information **Figure S1-S3**, showing similar results. Based on this it can be postulated that a high dielectric scaffold can suppress dendrite growth and promote a homogeneous and more dense Li-metal filling of the pores of the scaffold. This can be expected to lead to less "dead" Li-metal forming as well as a smaller Li-metal electrolyte interface, thus less electrolyte decomposition, enabling higher cycling efficiencies and longer cycle life of the Li-metal anode.

Electrode preparation. To evaluate the impact of the BTO and AO porous scaffolds, both materials were cast on a Cu current collector, similar to what is done in the preparation of regular Li-ion insertion electrodes. Commercial BTO and AO were ball-milled at 450 rpm for 20 hours to obtain a comparable size distribution of both materials. **Figure S4 a,c** shows the morphology of the BTO and AO particles obtained via a scanning electron microscopy (SEM) analysis. Both materials have an average particle size of approximately 8 µm as seen from the SEM images (**Figure S4**) and via a Dynamic Light Scattering (**Figure S5**) analysis. According to the nitrogen adsorption/desorption isotherms (**Figure S6**), their Brunauere-Emmette-Teller (BET) specific surface areas are also comparable, amounting 23.59 and 23.08 $m^2 g^{-1}$ for BTO and AO, respectively. The similar surface area and particle size distribution of BTO and AO are crucial to allow us to distinguish the impact of the dielectric constant on Li-metal deposition from that of the scaffold morphology. These ball-milled materials were used to build the scaffold for lithium metal plating on a Cu current collector. Both materials were mixed with polyvinylidene fluoride (PVDF) and NH_4HCO_3 (ratio at 5:1:4) using an N-methyl-2-pyrrolidone (NMP) solvent to obtain a slurry that was cast on a regular Cu current collector. The NH_4HCO_3 acts as a template to achieve a high porosity[33] which is required to achieve high specific anode capacities, taking into account the weight of the scaffold. After that, the electrodes were dried under vacuum at 80 °C to remove the NH_4HCO_3 template. The resulting porosity of the AO and BTO scaffolds is 62% and 64%, respectively and thus comparable. The thickness of these two electrodes is around 45 µm, including 10 µm copper foil. When this porous volume is completely filled by Li-metal, the specific capacity of the anode is approximately 2240 mAh g^{-1}. Aiming to expose the impact of a high dielectric scaffold on the cycle life of anode-less configuration of these electrodes, a blank 1M $LiPF_6$ in EC/DMC

electrolyte was used. As mentioned earlier, this represents a worst-case scenario because it is well known that this electrolyte formulation leads to uncontrolled dendrite and SEI formation.[9,34]

Operando solid-state NMR. To test the hypothesis that the Li-metal deposition is less dendritic and more homogeneous in the pores of the high dielectric scaffold, and that this leads to better reversibility, operando ^{7}Li solid-state NMR is performed, the results of which are shown in **Figure 2**. Operando ^{7}Li solid-state NMR is a direct probe of Li in realistic cell conditions and allows to distinguish differences in the Li-metal microstructure.[12,35,36] As shown in Supplementary **Figure S7**, the signals from Li-species in the SEI and electrolyte are in the expected region of diamagnetic materials (-10 to 10 ppm), Li in the $LiCoO_2$ (cathode) in the wide region of -50 to 50 ppm, which both can be readily separated from the Li-metal chemical shift which is dominated by its knight shift.[35] The NMR radiofrequency (RF) has a limited penetration depth into the Li-metal, referred to as skin depth, which at the presently employed **B₀** field of 11.7 T amounts to approximately 11 μm.[13] As a consequence, for deposited Li-microstructures such as dendrites and mossy structures, typically smaller than a few micrometres, the RF penetration can thus be expected to be complete. A Li-metal strip[13,35] gives rise to a resonance at ~245 ppm when placed perpendicular to the fixed magnetic field **B₀** and at ~270 ppm when the strip is parallel to **B₀**, a consequence of the bulk magnetic susceptibility effect.[13] An anode-less design (absence of Li-metal at the anode in the initial state) is investigated by operando solid-state NMR, utilizing $LiCoO_2$ as the counter electrode (and Li source), such that the observed Li-metal signal arises only due to the deposition at the anodes of interest, similar to a recently reported study[37].
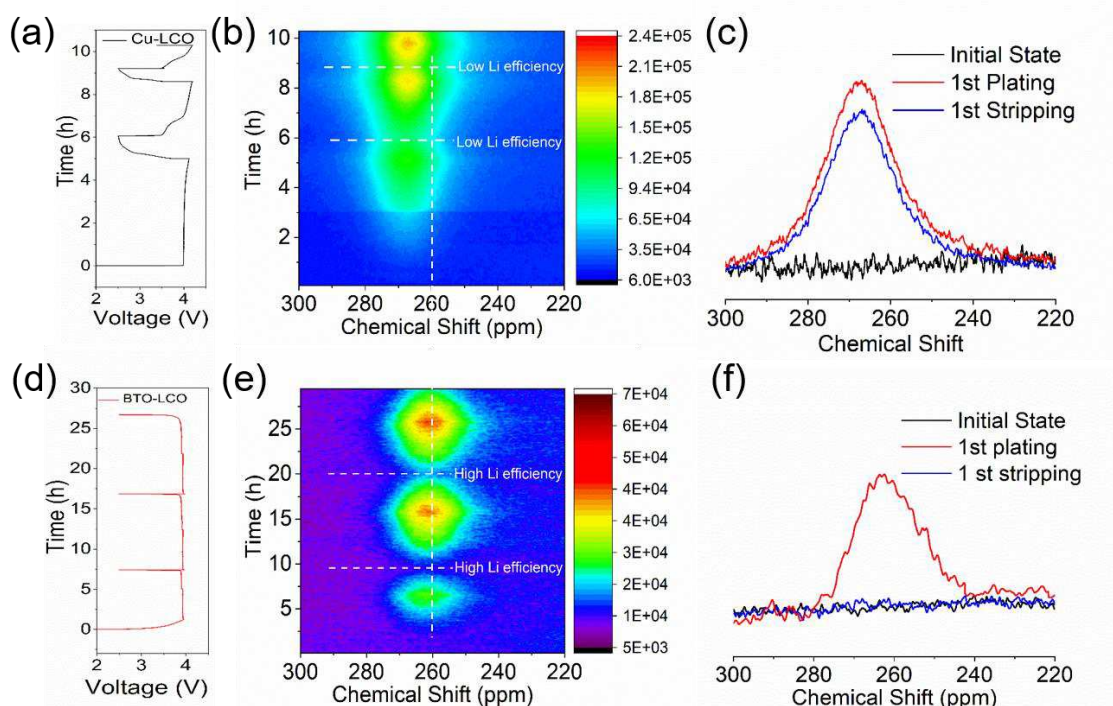
Figure 2. Operando ^{7}Li solid-state NMR of Li-metal plating/stripping on bare Cu and the anode-less BTO porous scaffold in a full cell versus LiCoO$_2$. (a-c) Bare Cu versus a LiCoO$_2$ cathode with a 1M LiPF$_6$ EC/DMC electrolyte cycled at 0.2 mA cm^{-2} to 1 mA cm^{-2} charge capacity and discharge to 2.5 V cut-off (a) voltage profile, (b) 2D ^{7}Li operando NMR spectra as a function of cycling, (c) 1D ^{7}Li solid-state NMR spectra at selected conditions. (d-f) Anode-less BTO scaffold on Cu versus a LiCoO$_2$ cathode with a 1M LiPF$_6$ EC/DMC electrolyte cycled at 0.2 mA cm^{-2} to 1 mA cm^{-2} charge capacity and discharge to 2.5 V cut-off (a) voltage profile, (b) 2D ^{7}Li operando NMR spectra as a function of cycling, (c) 1D ^{7}Li solid-state NMR spectra at selected conditions.

During charge (plating) on the bare Cu current collector, the ^{7}Li metal resonance appears at approximately 266 ppm as shown in **Figure 2b** and **2c**. On the other hand for the Li-metal deposits in the BTO scaffold, it occurs at approximately 260 ppm shown in **Figure 2e** and **2f**. Dendritic microstructures, growing perpendicular to Cu have been associated with a narrow chemical shifts range centred at around 270 ppm whereas mossy microstructures encompass broader resonances covering a chemical shift range of 262-274 ppm.[12] Not surprisingly, the present results demonstrate that on a bare Cu current collector, in combination with a regular carbonate electrolyte, mossy/dendritic Li-metal growth is initiated already during the first plating cycle.

Interestingly, the Li-metal chemical shift in the BTO scaffold is similar to that observed for dense Li-metal plated in the separator when plated under pressure.[12] The density of the BTO scaffold (64 %) is similar to that of the separators, thus the operando ^{7}Li solid-state NMR indicates that Li-metal plating fills the BTO scaffold pores, preventing the growth of mossy and dendritic microstructures. Discharge (Li-metal stripping) of the bare Cu current collector results in high overpotentials, indicating a strongly increased internal resistance, which is associated with severe SEI formation that hinders Li-ion transport as seen in **Figure 2a**. The intensity of the ^{7}Li metal NMR resonance hardly decreases during discharge (**Figure 2b** and **2c**), reflecting the difficulty to strip the Li-metal deposits from the Cu, which upon cycling results in rapid accumulation of inactive "dead" Li-metal (see **Figure 2b**) comprehensively studied recently using operando NMR.[37] In contrast, the voltage during discharge (Li-metal stripping) for the BTO scaffold is nearly the same as during charge, indicating that the internal resistance is practically unaffected by the SEI formation. Concurrently, the ^{7}Li metal resonance completely disappears upon the charge, as confirmed in **Figure 2f**, demonstrating that all Li-metal can be completely stripped from the BTO scaffold, and thus that a high Li-metal stripping/plating efficiency is achieved. The large increase in Li-metal signal after the first cycle can be explained by a low first cycle efficiency, where a significant fraction of the capacity is lost in the formation of SEI products by introducing Li-metal at the anode. In summary, operando ^{7}Li solid-state NMR demonstrates that the presence of the high dielectric anode-less BTO scaffold results in more compact and less dendritic/mossy Li-metal, in line with the suggested impact of a high dielectric scaffold on the electrical field gradients shown in **Figure 1,** which reduces the amount of observed "dead" Li-metal and SEI formation, even in a conventional 1 M LiPF$_6$ EC/DMC electrolyte.

Electrochemical evaluation half cells. Galvanostatic cycling in a half-cell is carried out to compare the reversibility of anode-less bare Cu with the porous BTO and AO scaffolds deposited on the Cu current collector, all in combination with a $LiPF_6$ in EC/DMC electrolyte. Coin cells were assembled using lithium foil as the counter-electrode to evaluate the cycling stability as expressed by the Coulombic Efficiency (CE) *i.e.* the ratio of the Li stripping capacity to the plating capacity, the results of which are shown in **Figure 3**.
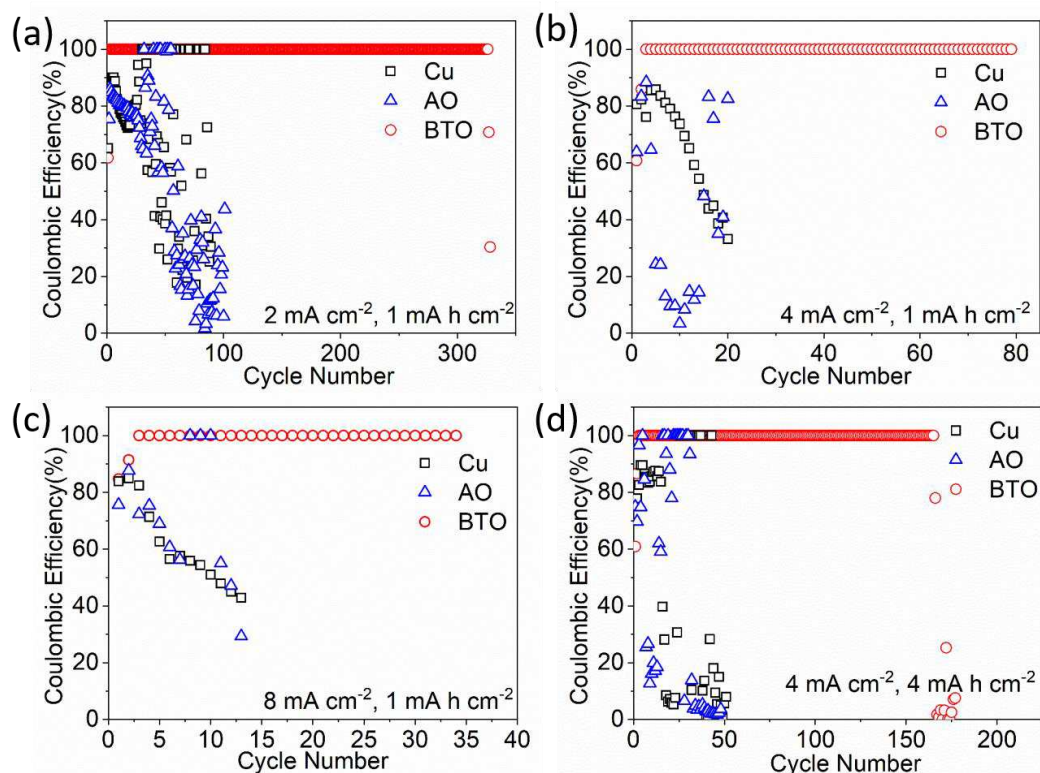

Figure 3 Half-cell performance of the anode-less Cu and AO and BTO scaffolds versus a Li-metal anode. (a-c) Lithium Coulombic efficiencies at a fixed areal capacity of 1 mA h cm⁻² at various current densities (a) 2 mA cm⁻², (b) 4 mA cm⁻², (c) 8 mA cm⁻² using three different electrodes. (d) Lithium Coulombic efficiency at a current density of 4 mA cm⁻² with a high areal capacity of 4 mA h cm⁻². For all experiments, the Li-metal stripping was cut off at 1.0 V vs Li/Li⁺.

The CE is an essential parameter to evaluate the reversibility of the lithium metal anode, reflecting the irreversible loss of Li to both "dead" Li (Li-metal electrically isolated from the current collector) and to the formation of the SEI species during each

cycle. Cycling is performed to a fixed Li-metal capacity of 1 mA h cm^{-2} at rates of 2, 4 and 8 mA cm^{-2} as shown in **Figure 3a-c**, and to a lithium metal capacity of 4 mA h cm^{-2} at a rate of 4 mA cm^{-2}, as shown in **Figure 3d**. Li-metal stripping is always limited by a 1.0 V vs Li/Li$^+$ cut-off voltage. The two initial cycles are always performed at a current density of 0.5 mA cm^{-2} to form the SEI, leading to a relatively low CE in the order of ~60% and ~85%. As shown in the cyclic voltammetry curves in **Figure S8**, the BTO scaffold shows a small peak at 1.2 V (and no activity is observed for AO). However, there is no obvious structural change of the BTO scaffold after the 1st and 100th cycles as verified by XRD (**Figure S9**). Therefore the BTO scaffold does contribute to the initial capacity loss. It does not, however, show degradation in contact with Li-metal and upon over cycling. Although both BTO and AO can be reduced by Li-metal, it appears that this process is passivated, most likely only occurring at the BTO/AO surface region. Under all cycling conditions, the BTO scaffold results in a dramatically improved CE and cycle life as compared to the bare Cu and the AO scaffold. After the two initial cycles, cycling to 1 mA h cm^{-2} at 2.0, 4.0 and 8.0 mA cm^{-2} results in a dramatically improved CE of 99.82%, 99.35%, and 99.30% for the cells with the BTO scaffold during 320, 80 and 30 cycles, respectively (**Figure 3a--c**). In sharp contrast, the cells with bare Cu and the AO scaffold show rapid decay in the cycling efficiency, leading to early cell death before reaching 20 cycles. Nevertheless, the BTO scaffold can maintain this for a limited number of cycles as indicated in **Figure 3**, which is remarkable given the non-optimized LiPF$_6$ EC/DMC electrolyte used. Also cycling towards a larger (practical) capacity of 4 mA h cm^{-2} at 4 mA cm^{-2}, which including the BTO scaffold equals a specific capacity of 2000 mA h g^{-1}, results in a CE of 99.68% that can be maintained for more than 160 cycles (**Figure 3d**). This is equivalent to a specific capacity above 2000 mA h g^{-1}, which in combination with a

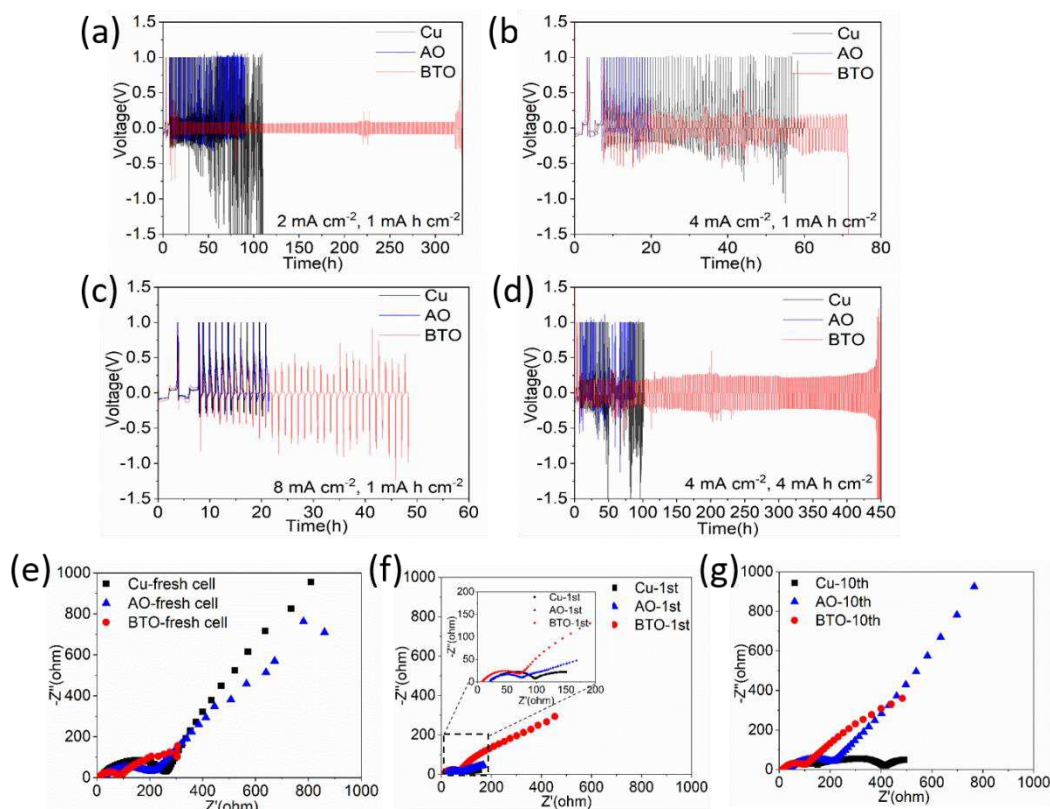sulphur-carbon cathode would yield a cell level energy density above 500 Wh kg^{-1}.

Figure 4 Half-cell voltage evolution and impedance of the anode-less Cu and AO and BTO scaffolds vs a Li-metal anode. Evolution of the voltage during Li plating/stripping for the bare Cu and the AO and BTO scaffolds at different current densities (a) 2 mA cm^{-2}, (b) 4 mA cm^{-2}, (c) 8 mA cm^{-2} with a fixed areal capacity of 1 mA h cm^{-2}, and (d) an increased areal capacity of 4 mA h cm^{-2} at a current density of 4 mA cm^{-2}. Electrochemical impedance spectra of the half-cells for the bare Cu and the AO and BTO scaffolds (e) fresh cells, (f) the 1st cycle and (g) the 100th cycle measured at a current density of 2 mA cm^{-2}.

The evolution of the voltage during cycling shown in **Figure 4** and **Figure S10** provides more insight into the evolution of the CE seen for the different anodes (**Figure 3**). Under all cycling conditions tested, the anode-less Cu and AO scaffold result in a rapid increase in the plating and stripping potentials as shown in **Figure 4a-d**. This can be associated with the SEI formation, amplified by mossy/dendritic Li-metal growth, leading a high internal resistance until no cycling capacity remains, or a short circuit results. The BTO scaffold can maintain much lower overpotentials for more cycles, *i.e.* approximately 68, 220 and 375 mV at current densities of 2, 4 and 8 mA cm^{-2}, respectively. Nevertheless, also for the BTO scaffold, the overpotentials increase,

14

indicating that upon extended cycling, these cells also fail due to SEI growth. These conclusions are further supported by electrochemical impedance spectroscopy (EIS) measurements shown in **Figure 4e-g**. The total resistance of the cells with the Cu and AO scaffold anode shows a strong increase after 100 cycles at 2 mA cm^{-2} shown in **Figure 4g**, associated with the SEI formation driven by mossy/dendritic Li-metal growth. At the same conditions, the BTO scaffold has a much lower interfacial resistance, indicating less SEI formation. In addition to half-cells, full cells were assembled using the BTO scaffold as a lithium free anode (anode-less), or a Li-metal anode, both paired with an NCM cathode, again in combination with a conventional 1 M LiPF$_6$ EC/DMC electrolyte (as shown in **Figure S11** and **S12**). The BTO scaffold outperforms the Li-metal anode in cycling rate and stability demonstrating a high average CE of 99.37%.

Li-metal morphology. An SEM analysis is performed before and after cycling the cells at a current density at 2 mA cm^{-2} to a specific capacity of 1 mA h cm^{-2}, comparing bare Cu, the low dielectric constant AO scaffold and the high dielectric constant BTO scaffold, shown in **Figure 5**. On comparison, the BTO scaffold appears to lead to a more uniform lithium deposition, as no dendritic/mossy structures are observed (**Figure 5b,e**). The cross-sectional SEM image of the BTO scaffold electrode(**Figure S13a**) also taken after plating to 1 mA h cm^{-2} at a current density of 2 mA cm^{-2}, suggests that the deposited Li-metal is dense and well-confined in the 3D scaffold of the BTO layer consistent with the operando ^{7}Li solid-state NMR measurements depicted in **Figure 2**. In contrast, Li deposition on the bare Cu foil exhibits islands of accumulated dendritic structures (**Figure 5a,d**) and at the surface of the AO scaffold, dendrites are observed (**Figure 5c,f**).
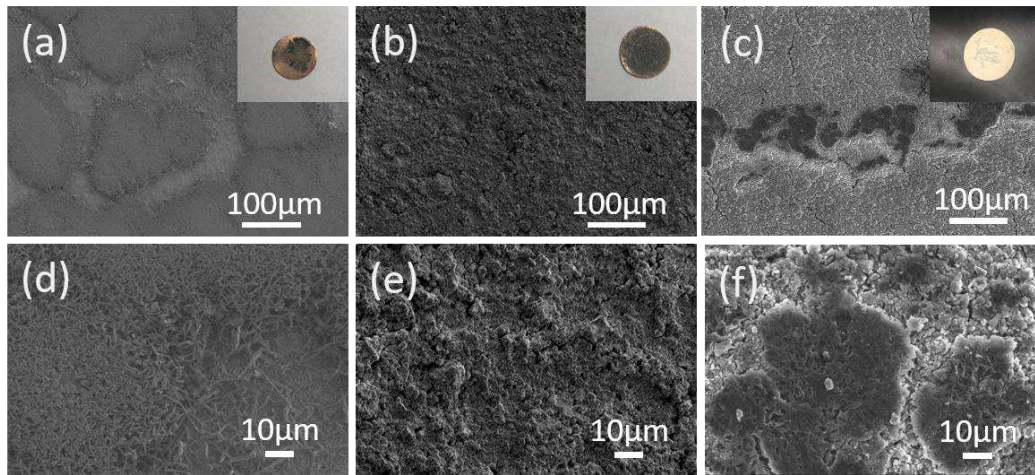
Figure 5 SEM images after plating to 1 mA h cm^{-2} at 2 mA cm^{-2} of the bare Cu, low dielectric AO scaffold and high dielectric BTO scaffold. (a, d) Bare copper electrode and zoomed-in figure, (b, e) high dielectric BTO scaffold and zoomed-in figure, (c, f) low dielectric AO scaffold and zoomed-in figure. Insets show the digital images of the complete electrodes.

Discussion and conclusions. As schematically shown in **Figure 6a**, a fundamental driving force for the formation of dendritic/mossy Li-metal are large gradients in the electrical field lines caused by surface inhomogeneities. This acts as the starting point for uncontrolled SEI formation which in turn amplifies further inhomogeneous mossy/dendritic Li-metal deposition and the accumulation of inactive Li-metal, as demonstrated by the operando solid-state NMR (**Figure 2**) and the SEM results (**Figure 5**). This drives up the internal resistance (**Figure 4**), eventually leading to cell death. A comparison of the high dielectric BTO scaffold ($\varepsilon_r \approx 4000$) and the low dielectric AO scaffold ($\varepsilon_r \approx 8$), having a similar morphology (in terms of loading, particle size distribution and porosity), makes it possible to distinguish between the impact of a non-conducting scaffold morphology and the impact of the dielectric constant of the scaffold on the Li-metal plating. As schematically shown in **Figure 6b**, the 3D high-dielectric BTO scaffold takes away the electrical field gradients at the tip of uneven Li-metal deposits, as supported by electrical field calculations (**Figure 1**). This leads to a more homogeneous Li-ion flux, and thus to less mossy/dendritic and more homogeneous Li-metal deposits as recently shown by Guo[32] and as evidenced by

16

operando solid-state NMR (**Figure 2**) and SEM (**Figure 5**). This prevents the accumulation of deactivated Li-metal which is responsible for the highly improved cycling efficiency (**Figure 3**) and lowers the exposed Li-metal-electrolyte area, minimizing SEI formation and thus preventing the uncontrolled and self-amplified growth of the SEI and dendritic Li-metal deposits, rationalizing the low overpotentials during extended cycling observed in **Figure 4**. As a result, the presented strategy enhances the cycle of life and lowers safety concerns associated with dendrite growth.[38] Notably, these results are achieved under the challenging conditions of an anode-less design i.e. the initial absence of Li-metal in the BTO scaffold, and in combination with a non-optimized carbonate electrolyte (1 M $LiPF_6$ EC/DMC).
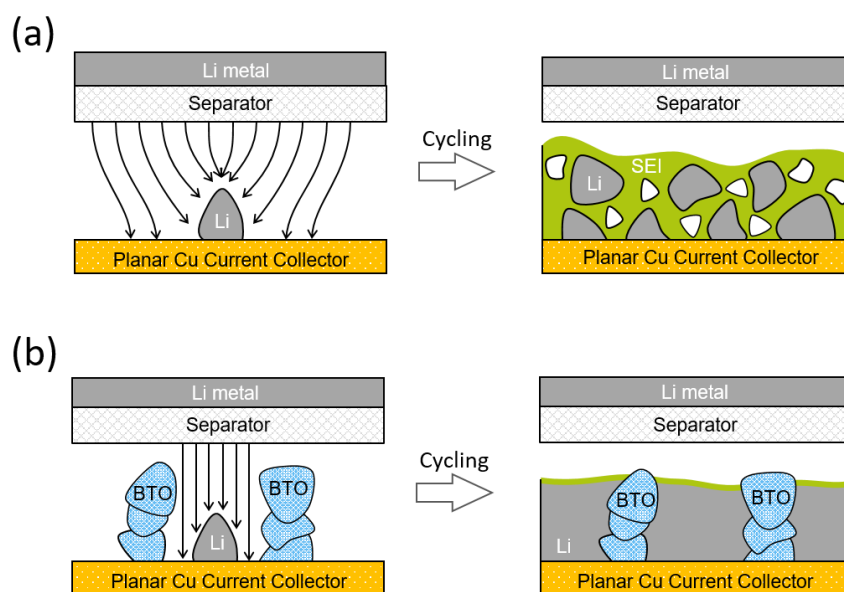

Figure 6 Schematic diagram of lithium metal plating and stripping with and without the presence of the high dielectric BTO porous scaffold. (a) lithium metal plating/stripping process on planer copper, (b) lithium metal plating/stripping process on BTO coated copper foil.

In conclusion, the challenge faced by Li-metal anodes is to prevent dendritic and mossy Li-metal growth that catalyse electrolyte decomposition and lead to low electrochemical plating/stripping efficiencies. Electrical field calculations show that through the ferroelectric effect, the presence of a high dielectric material takes away

the electrical field gradient at the tip of nearby Li-metal deposits, suggesting that the Li-metal dendritic and mossy microstructure growth can be suppressed by an anode comprising of a high dielectric porous scaffold. 3D porous scaffolds are prepared through a facile casting approach using both a high dielectric scaffold material, $BaTiO_3$ (BTO) and a low dielectric scaffold material, Al_2O_3 (AO), to distinguish between the impact of a porous scaffold and the high dielectric constant on the electrochemical Li-metal plating. These electronically insulating scaffolds show minimal electrochemical activity, and the added weight leads to specific capacities exceeding 2000 mA h g^{-1}. Operando ^7Li solid-state NMR of an anode-less BTO scaffold-$LiCoO_2$ full cell demonstrates that the high dielectric scaffold induces compact plating and efficient stripping. Half-cells with a BTO scaffold cycled against Li-metal exhibits 99.82% CE after the first two initial cycles, low overpotentials and an extended cycle life in when the worst-case scenario 1 M $LiPF_6$ EC/DMC electrolyte is used, under different current and capacity conditions. With the same basic electrolyte, full cells also demonstrate improved performance with an average CE of 99.37%. These results demonstrate the use of high dielectric scaffolds that take away the driving force for inhomogeneous Li-metal deposition as a strategy to improve the reversibility and safety of Li-metal anodes in an anode-less configuration. The next avenues to explore are combinations with more stable SEI forming electrolytes and additives, optimization of the high dielectric scaffold, to minimize the capacity loss during the first cycles and to further extend the cycle life.

Methods

Preparation of electrodes and electrochemical tests. Commercial $BaTiO_3$ (Euro Support Advanced Materials B.V., denoted as BTO) and Al_2O_3 (Sigma-Aldrich,

denoted as AO) powder were used to prepare 3D scaffolds on Cu current collectors having a high relative permittivity ($\varepsilon_r \approx 4000$) and a low relative permittivity ($\varepsilon_r \approx 8$) respectively. Firstly, BTO and AO were ball-milled at 450 rpm, 6 hours using 10 ZrO_2 balls to achieve relatively small particles and similar particle size distribution. Both materials were mixed with polyvinylidene fluoride(PVDF) and NH_4HCO_3 (ratio at 5:1:4) using N-methyl-2-pyrrolidone (NMP) solvent to obtain a slurry which is casted on copper. The NH_4HCO_3 acts as a template to achieve a high porosity[33] to increase the specific capacity of the anode (BTO scaffold). After that, the electrodes were dried under vacuum at 80 °C to remove the NH_4HCO_3 template. The resulting electrodes were cut into round electrodes with a diameter of 12.7 mm. Coin cells were assembled using as-prepared electrodes with lithium metal as a counter electrode, a PE (Celgard 2300) separator and 150 µl conventional carbonate electrolyte (1M $LiPF_6$ in 1:1 v/v EC: DMC). Galvanostatic cycling was performed by deposition of Li onto the bare Cu working electrode or AO/BTO coated Cu scaffolds with different current densities (2 mA cm^{-2} to 8 mA cm^{-2}) to a fixed capacity (1 mA h cm^{-2} or 4 mA h cm^{-2}), followed by complete Li stripping at different current densities up to a voltage cutoff of 1.0 V vs Li/Li$^+$. A rest time of 2-30 minutes was set between plating and stripping. Full cells composed of a porous BTO scaffold on a Cu current collector (denoted as BTOCu) in combination with a $LiNi_{0.8}Co_{0.1}Mn_{0.1}O_2$ (Umicore N.V., denoted as NCM) cathode were assembled. The BTO scaffold anode was firstly cycled versus Li-metal for two cycles to minimize initial irreversible Li consumption. NCM and $LiCoO_2$ (Sigma-Aldrich, denoted as LCO) cathodes were prepared by mixing the active material with Super P and PVDF in a mass ratio of 8:1:1, and NMP was used as a solvent. The mass loading of the NCM/LCO electrode was ~5 mg cm^{-2}. Li/NCM and BTOCu/NCM cells were cycled within the potential range of 3.0 - 4.2 V (vs. Li/Li$^+$) at room temperature. Galvanostatic cycling was conducted on a Maccor battery testing system. The impedance measurements of the coin cells were carried out on Autolab between 100 kHz and 0.01 Hz. Cyclic voltammograms (CVs) were recorded using the same electrochemical workstation at a scan rate of 1 mV s^{-1} in the range of -0.5 V - 3 V.

Characterization of the Materials and the Electrodes. SEM images were obtained of the 3D scaffolds after a discharge capacity of 1 mA h cm^{-2}. Before SEM imaging, the electrodes were rinsed with dimethyl carbonate in a glove box to remove lithium salts and dried several times in a vacuum chamber. Cross-section SEM samples were

prepared by cutting with scissors in the glove box. Subsequently, samples were transferred into an SEM (JEOL JSM-6010LA) machine under dry Argon conditions, and images were taken using an accelerating voltage of 2-10 kV (secondary electron). Nitrogen adsorption-desorption isotherms were recorded using an automatic surface area and porosity analyzer (Micromeritics) at 77 K. The particle size distribution of BTO and AO after ball milling was measured using Microtrac S3500.

LCO/Cu and LCO/BTOCu cells (in a plastic cell capsule suitable for operando NMR measurements and reported in detail elsewhere)[39] with a conventional carbonate electrolyte were assembled in the glove box and studied by operando ^{7}Li-NMR to monitor the microstructural evolution of Li deposits. Measurements were done on a wide bore Bruker Ascend 500 system equipped with a NEO console with a magnetic field strength of 11.7T and a ^{7}Li resonance frequency of 194.37 MHz. Operando static ^{7}Li NMR experiments were performed at room temperature with an NMR Service ATMC operando NMR probe, and the electrochemical cell was simultaneously controlled by a portable Maccor battery testing system. During the 1D static ^{7}Li NMR measurements the cells were charged to 1 mA cm^{-2} at 0.2 mA cm^{-2} to deposit Li to the anode and subsequently discharged 2.5 V to stripped the Li-metal from the anode, while the NMR spectra were continuously acquired. Each spectrum took ~2 minutes to acquire. The chemical shifts are referenced to a 0.1M LiCl solution. Bruker Topspin 4.0.6 as well as Mestrenova were used for raw data processing and analysis.

Electrical field calculations. All simulations were done in COMSOL Multiphysics 5.4. Using the electrostatics software, the electric field around a simulated dendrite was calculated. The electrodes used were copper and lithium which were taken from the COMSOL material's library. Three different electrodes are considered, bare Cu and Cu with different insulator blocks (BTO, AO). Two electrodes (Cu (2 µm x 250 µm) versus BTO on Cu, or AO on Cu (2 µm x 250 µm)) were placed at two sides of the electrolyte (EC/DMC, 50 µm x 250 µm). The BTO and AO blocks on the electrode have the dimensions 8 µm x 8 µm with a gap of 2 µm. For the simulations, a dendrite is represented as a rectangular shape (0.1 µm x 0.2 µm) with a hemispherical top. The dielectric constants or equivalent the relative permittivity of the BTO, AO and the electrolyte EC/DMC is 4000, 8 and 40, respectively.

References

1   Armand, M. & Tarascon, J.-M. Building better batteries. *Nature* **451**, 652-657 (2008).

2   Goodenough, J. B. & Park, K. S. The Li-ion rechargeable battery: a perspective. *J. Am. Chem. Soc.* **135**, 1167-1176 (2013).

3   Dunn, B., Kamath, H. & Tarascon, J.-M. Electrical energy storage for the grid: a battery of choices. *Science* **334**, 928-935 (2011).

4   Tarascon, J.-M. & Armand, M. Issues and challenges facing rechargeable lithium batteries. *Nature* **414**, 359-367 (2001).

5   Qiao, Y., Deng, H., He, P. & Zhou, H. A 500 Wh/kg Lithium-Metal Cell Based on Anionic Redox. *Joule* **4**, 1445-1458 (2020).

6   Xu, W. *et al.* Lithium metal anodes for rechargeable batteries. *Energy Environ. Sci.* **7**, 513-537 (2014).

7   Lin, D., Liu, Y. & Cui, Y. Reviving the lithium metal anode for high-energy batteries. *Nat. Nanotech.* **12**, 194 (2017).

8   Guo, Y., Li, H. & Zhai, T. Reviving lithium-metal anodes for next-generation high-energy batteries. *Adv. Mater.* **29**, 1700007 (2017).

9   Cheng, X.-B., Zhang, R., Zhao, C.-Z. & Zhang, Q. Toward safe lithium metal anode in rechargeable batteries: a review. *Chem. Rev.* **117**, 10403-10473 (2017).

10   Zhang, X., Wang, A., Liu, X. & Luo, J. Dendrites in lithium metal anodes: suppression, regulation, and elimination. *Acc. Chem. Res.* **52**, 3223-3232 (2019).

11   Hsieh, Y.-C. *et al.* Quantification of Dead Lithium via In Situ Nuclear Magnetic Resonance Spectroscopy. *Cell Rep. Phys. Sci.* **1**, 100139 (2020).

12   Chang, H. J. *et al.* Investigating Li microstructure formation on Li anodes for lithium batteries by in situ ^{6}Li/^{7}Li NMR and SEM. *J. Phys. Chem. C* **119**, 16443-16451 (2015).

13   Bhattacharyya, R. *et al.* In situ NMR observation of the formation of metallic lithium microstructures in lithium batteries. *Nat. Mater.* **9**, 504-510 (2010).

14   Märker, K., Xu, C. & Grey, C. P. Operando NMR of NMC811/graphite lithium-ion batteries: Structure, dynamics, and lithium metal deposition. *J. Am. Chem. Soc.* **142**, 17447-17456 (2020).

15   Weber, R. *et al.* Long cycle life and dendrite-free lithium morphology in anode-free lithium pouch cells enabled by a dual-salt liquid electrolyte. *Nat. Energy* **4**, 683-689 (2019).

16   Tikekar, M. D., Choudhury, S., Tu, Z. & Archer, L. A. Design principles for electrolytes and interfaces for stable lithium-metal batteries. *Nat. Energy* **1**, 1-7 (2016).

17   Lang, J., Qi, L., Luo, Y. & Wu, H. High performance lithium metal anode: progress and prospects. *Energy Stor. Mater.* **7**, 115-129 (2017).

18   Chazalviel, J.-N. Electrochemical aspects of the generation of ramified metallic electrodeposits. *Phys. Rev. A* **42**, 7355 (1990).

19   Ely, D. R. & García, R. E. Heterogeneous nucleation and growth of lithium electrodeposits on negative electrodes. *J. Electrochem. Soc.* **160**, A662 (2013).

20   Yan, K. *et al.* Selective deposition and stable encapsulation of lithium through heterogeneous seeded growth. *Nat. Energy* **1**, 1-8 (2016).

21   Ling, C., Banerjee, D. & Matsui, M. Study of the electrochemical deposition of Mg in the atomic level: why it prefers the non-dendritic morphology. *Electrochim. Acta* **76**, 270-274 (2012).

22   Wang, J. *et al.* In Situ Self-Assembly of Ordered Organic/Inorganic Dual-Layered Interphase for Achieving Long-Life Dendrite-Free Li Metal Anodes in LiFSI-Based Electrolyte. *Adv. Funct. Mater.* 2007434 (2020).

23   Wang, X. *et al.* Stress-driven lithium dendrite growth mechanism and dendrite mitigation by electroplating on soft substrates. *Nat. Energy* **3**, 227 (2018).

24   Monroe, C. & Newman, J. Dendrite growth in lithium/polymer systems: A propagation model for liquid electrolytes under galvanostatic conditions. *J. Electrochem. Soc.* **150**, A1377 (2003).

25   Zhang, R. *et al.* Conductive nanostructured scaffolds render low local current density to inhibit lithium dendrite growth. *Adv. Mater.* **28**, 2155-2162 (2016).

26   Liu, Y. *et al.* Lithium-coated polymeric matrix as a minimum volume-change and dendrite-free lithium metal anode. *Nat. Commun.* **7**, 10992 (2016).

27   Liang, Z. *et al.* Composite lithium metal anode by melt infusion of lithium into a 3D conducting scaffold with lithiophilic coating. *Proc. Natl. Acad. Sci. USA* **113, 2862** (2016).

28   Chi, S. S., Liu, Y., Song, W. L., Fan, L. Z. & Zhang, Q. Prestoring lithium into stable 3D nickel foam host as dendrite-free lithium metal anode. *Adv. Funct. Mater.* **27**, 1700348 (2017).

29   Zhang, Y. *et al.* High-capacity, low-tortuosity, and channel-guided lithium metal anode. *Proc. Natl. Acad. Sci. USA* **114, 3584** (2017).

30   Yun, Q. *et al.* Chemical dealloying derived 3D porous current collector for Li metal anodes. *Adv. Mater.* **28**, 6932-6939 (2016).

31   Fan, L. *et al.* Stable Lithium Electrodeposition at Ultra-High Current Densities Enabled by 3D PMF/Li Composite Anode. *Adv. Energy Mater.* **8**, 1703360 (2018).

32   Guo, Y. *et al.* Shaping Li Deposits from Wild Dendrites to Regular Crystals via the Ferroelectric Effect. *Nano Lett.* **20**, 7680-7687 (2020).

33   Singh, D. P., Mulder, F. M. & Wagemaker, M. Templated spinel $Li_4Ti_5O_{12}$ Li-ion battery electrodes combining high rates with high energy density. *Electrochem. Commun.* **35**, 124-127 (2013).

34   Liu, D.-H. *et al.* Developing high safety Li-metal anodes for future high-energy Li-metal batteries: strategies and perspectives. *Chem. Soc. Rev.* **49**, 5407-5445 (2020).

35   Marbella, L. E. *et al.* ^{7}Li NMR chemical shift imaging to detect microstructural growth of lithium in all-solid-state batteries. *Chem. Mater.* **31**, 2762-2769 (2019).

36   Bayley, P. M., Trease, N. M. & Grey, C. P. Insights into electrochemical sodium metal deposition as probed with in situ ^{23}Na NMR. *J. Am. Chem. Soc.* **138**, 1955-1961 (2016).

37   Gunnarsdóttir, A. B., Amanchukwu, C. V., Menkin, S. & Grey, C. P. Noninvasive In Situ NMR Study of "Dead Lithium" Formation and Lithium Corrosion in Full-Cell Lithium Metal Batteries. *J. Am. Chem. Soc.* (2020).

38   Zhang, W., Zhuang, H. L., Fan, L., Gao, L. & Lu, Y. A "cation-anion regulation" synergistic anode host for dendrite-free lithium metal batteries. *Sci. Adv.* **4, eaar4410** (2018).

39   Pecher, O., Carretero-González, J., Griffith, K. J. & Grey, C. P. Materials' methods: NMR in battery research. *Chem. Mater.* **29**, 213-242 (2017).

Author contributions

M.W. conceived the research, M.W. and C.W. designed the experiments. C.W. carried out materials and electrochemical characterization. M.L. and S.G. conducted NMR experiments and data analysis. M.T. performed the electric field simulations. F.O. participated in part of the electrochemical characterization. M.W. C.W. and M.L. co-wrote the paper. C.W. and M.L. contributed equally to this work. All authors discussed the results and commented on the manuscript.

Additional information

Supplementary information is available online.

Competing interests

The authors declare no competing financial interests.

Figures

Figure 1

Electrical field simulations around a Li-metal deposit with and without the presence of low and high dielectric blocks. Li-metal deposit (a) on bare Cu planar copper and (b) zoomed-in figure, (c) in combination with low dielectric AO block (d) zoomed-in figure, (e) in combination with high dielectric BTO block (f) zoomed-in figure.
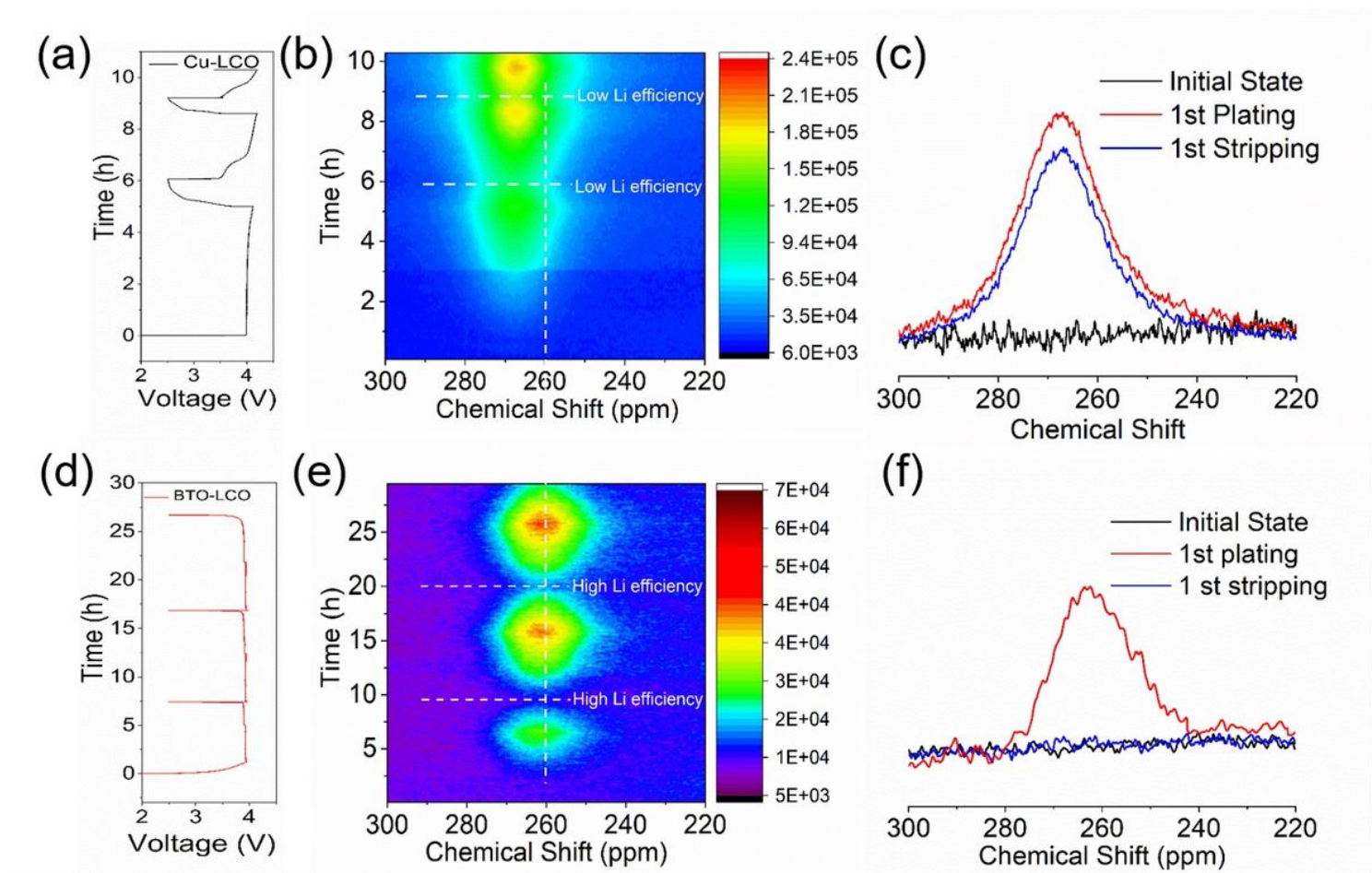
Figure 2

Operando 7Li solid-state NMR of Li-metal plating/stripping on bare Cu and the anode-less BTO porous scaffold in a full cell versus LiCoO2. (a-c) Bare Cu versus a LiCoO2 cathode with a 1M LiPF6 EC/DMC electrolyte cycled at 0.2 mA cm-2 to 1 mA cm-2 charge capacity and discharge to 2.5 V cut-off (a) voltage profile, (b) 2D 7Li operando NMR spectra as a function of cycling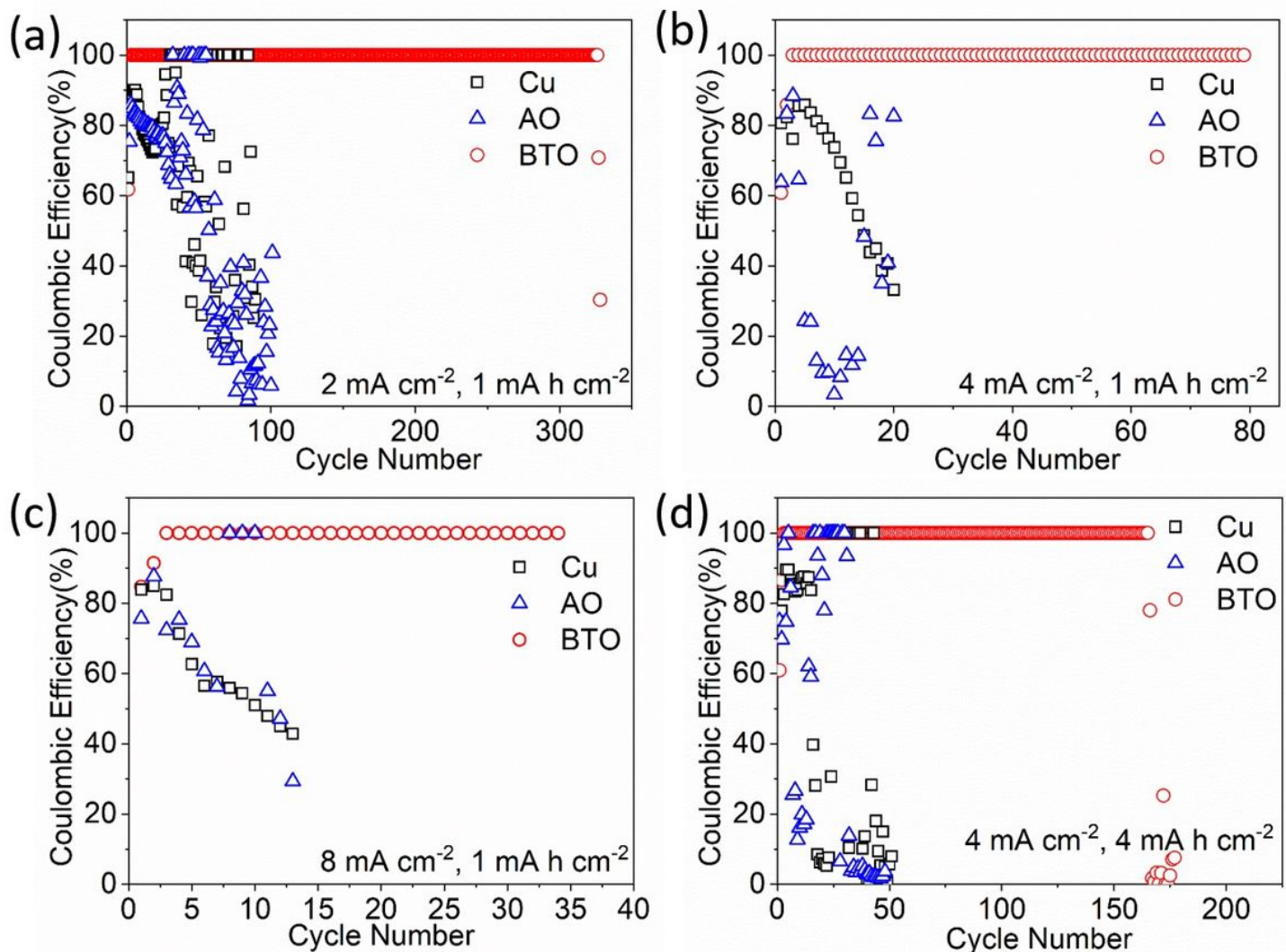, (c) 1D 7Li solid-state NMR spectra at selected conditions. (d-f) Anode-less BTO scaffold on Cu versus a LiCoO2 cathode with a 1M LiPF6 EC/DMC electrolyte cycled at 0.2 mA cm-2 to 1 mA cm-2 charge capacity and discharge to 2.5 V cut-off (a) voltage profile, (b) 2D 7Li operando NMR spectra as a function of cycling, (c) 1D 7Li solid-state NMR spectra at selected conditions.

Figure 3

Half-cell performance of the anode-less Cu and AO and BTO scaffolds versus a Li-metal anode. (a-c) Lithium Coulombic efficiencies at a fixed areal capacity of 1 mA h cm-2 at various current densities (a) 2 mA cm-2, (b) 4 mA cm-2, (c) 8 mA cm-2 using three different electrodes. (d) Lithium Coulombic efficiency at a current density of 4 mA cm-2 with a high areal capacity of 4 mA h cm-2. For all experiments, the Li-metal stripping was cut off at 1.0 V vs Li/Li+.
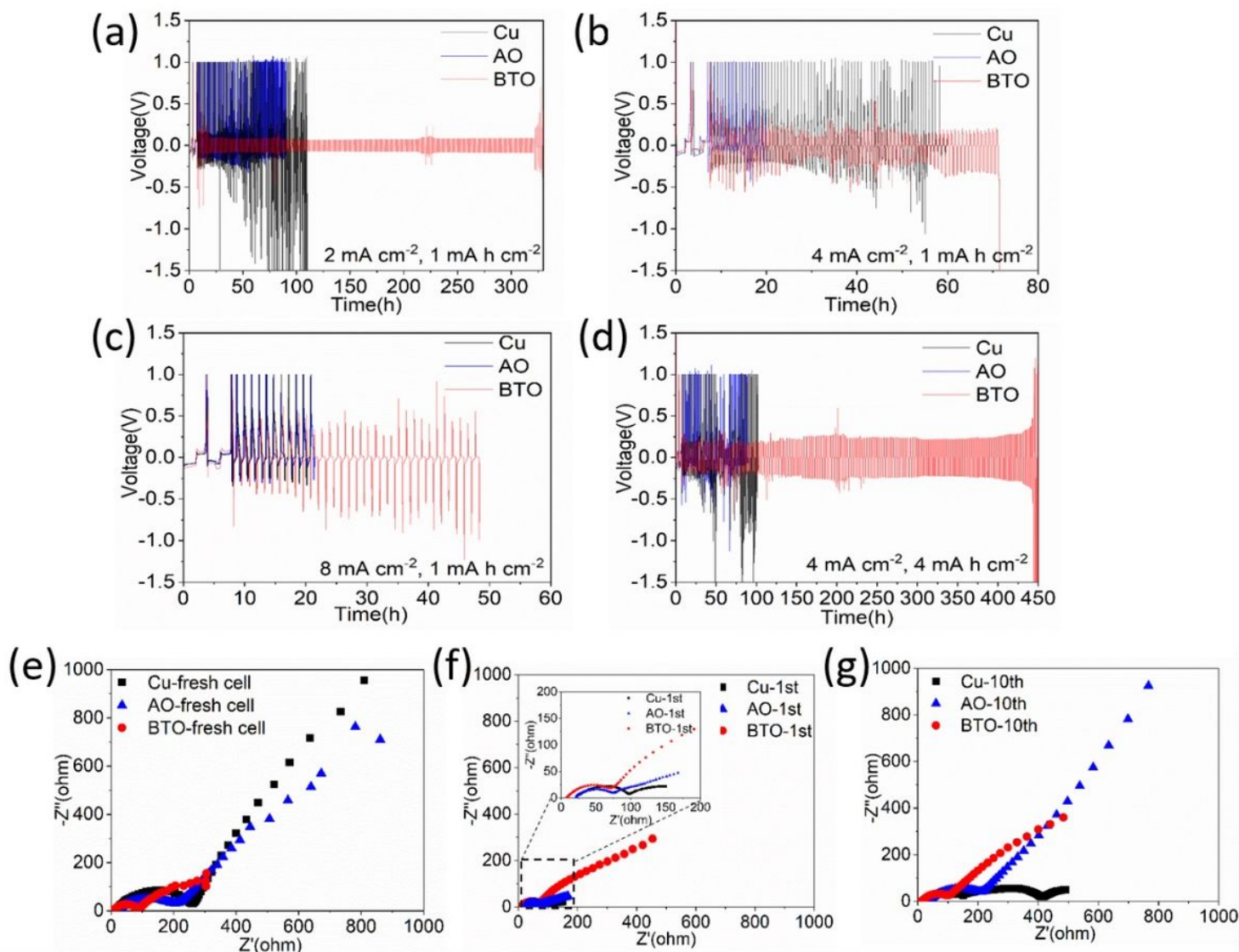
Figure 4

Half-cell voltage evolution and impedance of the anode-less Cu and AO and BTO scaffolds vs a Li-metal anode. Evolution of the voltage during Li plating/stripping for the bare Cu and the AO and BTO scaffolds at different current densities (a) 2 mA cm-2, (b) 4 mA cm-2, (c) 8 mA cm-2 with a fixed areal capacity of 1 mA h cm-2, and (d) an increased areal capacity of 4 mA h cm-2 at a current density of 4 mA cm-2. Electrochemical impedance spectra of the half-cells for the bare Cu and the AO and BTO scaffolds (e) fresh cells, (f) the 1st cycle and (g) the 100th cycle measured at a current density of 2 mA cm-2.
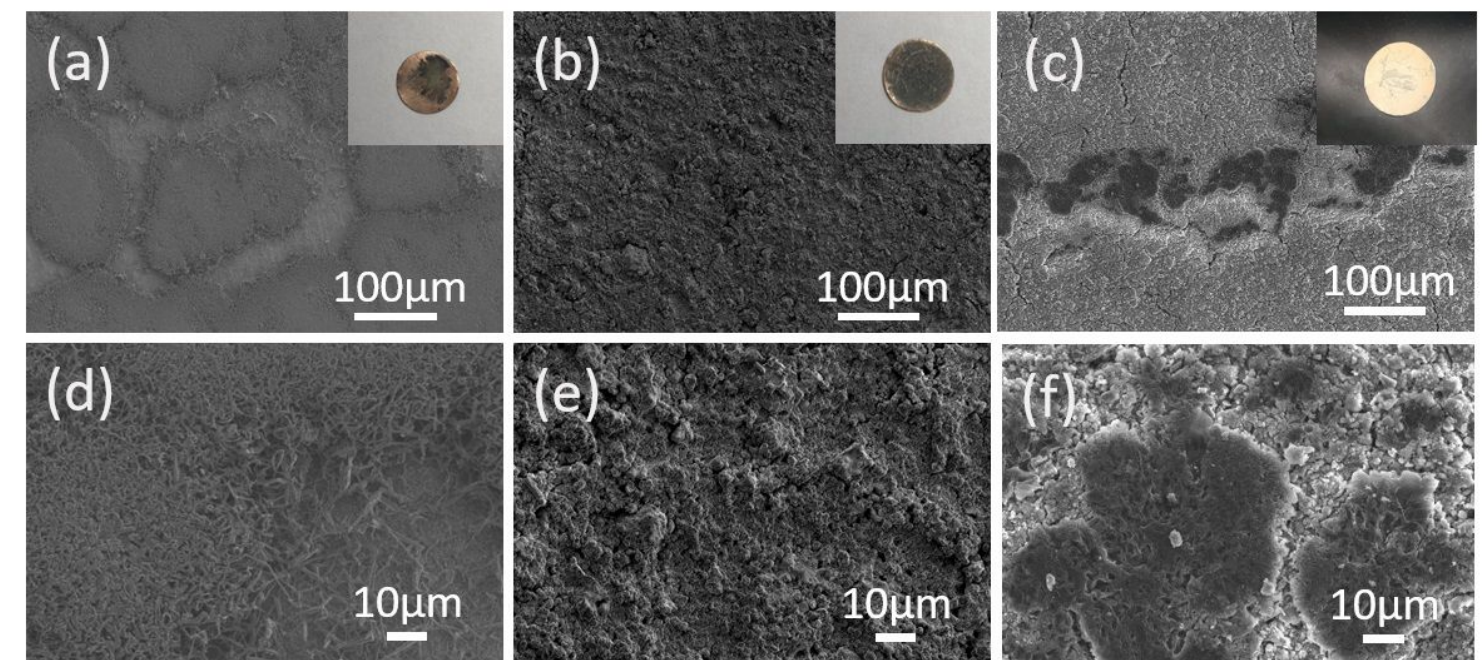
Figure 5

SEM images after plating to 1 mA h cm-2 at 2 mA cm-2 of the bare Cu, low dielectric AO scaffold and high dielectric BTO scaffold. (a, d) Bare copper electrode and zoomed-in figure, (b, e) high dielectric BTO scaffold and zoomed-in figure, (c, f) low dielectric AO scaffold and zoomed-in figure. Insets show the digital images of the complete electrodes.
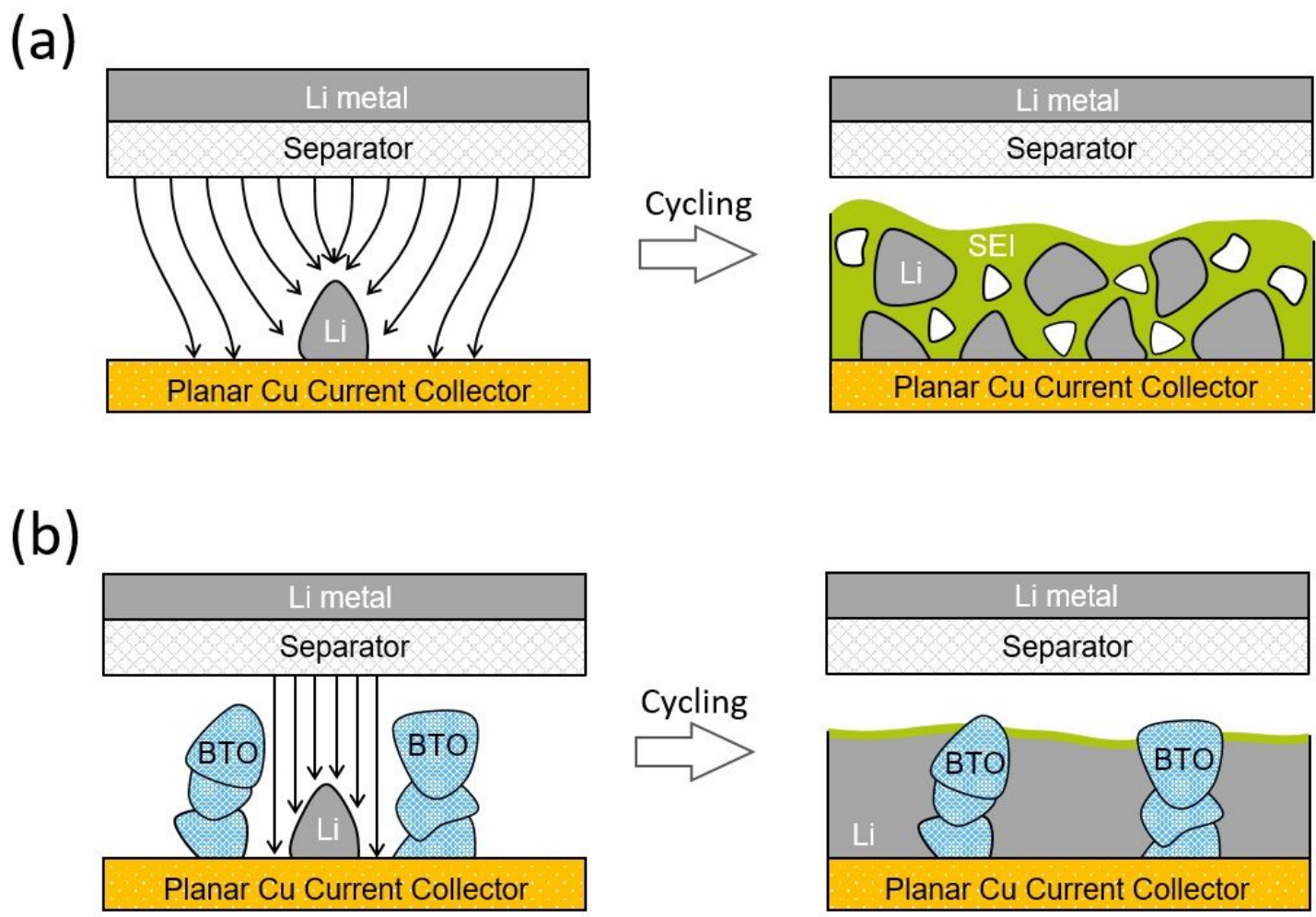
Figure 6

Schematic diagram of lithium metal plating and stripping with and without the presence of the high dielectric BTO porous scaffold. (a) lithium metal plating/stripping process on planer copper, (b) lithium metal plating/stripping process on BTO coated copper foil.

Supplementary Files

This is a list of supplementary files associated with this preprint. Click to download.

- LiquidBTOSI.docx